PAPER • OPEN ACCESS

The synergistic effect of deuterium and helium on the microstructure evolution of W–Y_2O_3 material during plasma exposure

To cite this article: Meiye Pan *et al* 2025 *Nucl. Fusion* **65** 076002

View the article online for updates and enhancements.

You may also like

- The topology of non-resonant stellarator divertors
Robert Davies, Christopher B. Smiet, Alkesh Punjabi et al.
- A high performance and dense Fe–Al/Al_2O_3 tritium permeation barrier coating prepared on 316LSS at low temperature
Bin Luo, Shijian Lin, Yinghong Li et al.
- Investigation of microstructural evolution of irradiation-induced defects in tungsten: an experimental–numerical approach
Salahudeen Mohamed, Qian Yuan, Dimitri Litvinov et al.

This content was downloaded from IP address 216.73.216.56 on 19/11/2026 at 09:12

OPEN ACCESS
IOP Publishing | International Atomic Energy Agency
Nuclear Fusion
Nucl. Fusion **65** (2025) 076002 (17pp)
https://doi.org/10.1088/1741-4326/addb5e

The synergistic effect of deuterium and helium on the microstructure evolution of W–Y_2O_3 material during plasma exposure

Meiye Pan[1], Lipeng Sun[1], Yifan Zhang[1,2,*], Jing Wang[1], Laima Luo[1,2] and Yucheng Wu[1,2,*]

[1] School of Materials Science and Engineering, Hefei University of Technology, Hefei 230009, China
[2] Engineering Research Center of High-Performance Copper Alloy Materials and Processing, Ministry of Education, Hefei 230009, China

E-mail: yfzhang@hfut.edu.cn and ycwu@hfut.edu.cn

Received 19 January 2025, revised 2 May 2025
Accepted for publication 21 May 2025
Published 30 May 2025

Abstract

This study presents a systematic investigation of the synergistic effect of deuterium and helium on the microstructural evolution of W–Y_2O_3 material during plasma exposure. The effect of single D/He and sequential D/He, He/D plasma exposure on the stability of Y_2O_3 nanoparticles and the microstructural evolution of the W matrix were investigated using scanning electron microscopy and transmission electron microscopy. The results indicate that Y_2O_3 particles undergo a significant size change during plasma exposure, and this process was significantly influenced by the synergistic effects of hydrogen and helium. The size evolution of Y_2O_3 particles is controlled by three mechanisms: the etching-controlled process at the initial stage, followed by deposition-controlled process or mixed-controlled processes. Interestingly, the fuzz structure on the surface of Y_2O_3 particles is proved to be W instead of Y_2O_3, which results from the deposition during plasma exposure. Significant synergistic effects of deuterium and helium were observed, in which the strong combination of H and He-vacancy composites suppressed the bubble formation and growth, leading to a different evolutionary dynamic.

Keywords: W–Y_2O_3, plasma exposure, H/He synergistic effect, microstructure stability

(Some figures may appear in colour only in the online journal)

* Authors to whom any correspondence should be addressed.

Original content from this work may be used under the terms of the Creative Commons Attribution 4.0 licence. Any further distribution of this work must maintain attribution to the author(s) and the title of the work, journal citation and DOI.

 © 2025 The Author(s). Published by IOP Publishing Ltd on behalf of the IAEA

1. Introduction

Tungsten (W) is considered as the primary candidate for plasma-facing materials in future fusion reactors due to its high melting point, excellent thermal conductivity, low sputtering rate, and minimal tritium retention [1, 2]. Recently, new tungsten-based materials, such as oxide dispersion-strengthened tungsten, have been proposed to overcome their shortcomings, especially the high ductile-to-brittle transition temperature, poor ductility, recrystallization brittleness, and irradiation embrittlement [3–5]. Recent studies indicate that W–Y_2O_3 has enhanced resistance to plasma exposure. Yao *et al* [6] found that the surface roughness of the W–2% Y_2O_3 material was lower than that of pure W after helium plasma irradiation. Lv *et al* [7] observed changes in the surface morphology of both pure tungsten and W–Y_2O_3 under the same irradiation energy but with different irradiation doses. They found that the irradiation dose required for surface changes in W–0.3%wt Y_2O_3 was higher than that for pure tungsten, suggesting that W–Y_2O_3 exhibits good radiation resistance.

Studies on the resistance of W–Y_2O_3 materials to plasma damage have primarily focused on the damage evolution processes in the tungsten matrix, including the formation of bubbles, waves, holes, fuzz and so on. The emergence of fuzz structures poses a significant challenge, as it notably diminishes surface stability and thermal conductivity. The removal of these fuzz structures adversely affects the stability of the core plasma [8]. However, investigations into the damage and evolution of Y_2O_3 particles are still limited. Yao *et al* [9] found that, with helium ion irradiation at a dose of 1.5×10^{26} ions m^{-2}, only a small number of micron-sized Y_2O_3 particles remained near the phase interfaces. Huang *et al* [10] found that the W matrix and Y_2O_3 particles exhibit different responses to helium plasma exposure. Specifically, fuzz formation occurs only on the W substrates, while Y_2O_3 particles develop nano-protrusions and small cracks on the surface and are unable to form fuzz structures autonomously.

These research results mainly examine the effects of the single H/He plasma exposure, with limited exploration of the synergistic impacts of H and He. The research of pure W and W-based alloy shows that H/He plasma exposure not only causes damage to tungsten, but also results in a significant synergistic effect during the damage evolution [11]. Helium bubbles may act as trap sites for H atoms and affect the retention of H isotopes in W [12]. H atoms in He pre-injected W tend to accumulate in He-saturated layers, and the presence of helium limits the diffusion of H in W. Liu *et al* [13] found that exposure to single H plasma only induced surface roughening due to physical sputtering, while exposure to mixed H/He plasma resulted in additional pinhole-like surface structures. Therefore, the synergistic effect of H/He plasma on the evolution of W–Y_2O_3 materials is worth further investigation.

Besides, most research about W–Y_2O_3 materials focuses on the evolution of the W matrix, neglecting the stability of Y_2O_3 particles. During long-term service, the evolution of particles is related to the microstructure and performance stability of W–Y_2O_3 materials and should not be ignored. In this work, the microstructure evolution of W–Y_2O_3 materials under single and mixed H/He plasma exposure, including the W matrix and Y_2O_3 particles, was studied using scanning electron microscopy (SEM) and transmission electron microscopy (TEM). The synergistic effect of deuterium and helium on the stability of Y_2O_3 particles and the evolution of fuzz structure were studied.

2. Experiment

2.1. Materials

The W–Y_2O_3 materials with a 0.5% weight percentage of Y_2O_3 were used in this experiment, which were prepared using the wet chemical method. Firstly, ammonium paratungstate (AMT, purity: $\geqslant$99.95%) and yttrium nitrate hexahydrate ($Y(NO_3)_3{\cdot}6H_2O$, purity: $\geqslant$99.5%) were selected as the raw materials for W and Y_2O_3, respectively, and oxalic acid ($C_2H_2O_4 \cdot 2H_2O$) was chosen as the precipitant to obtain the W–Y_2O_3 precursor. The precursors were then subjected to powder reduction with a loading of 1 kg per combustion boat and the flow rate of hydrogen during the reduction process was maintained at 24 $m^3\ h^{-1}$. The temperature range of the hydrogen reduction furnace was 880 °C–930 °C with three temperature zones. The combustion boat slowly passes through the three temperature zones under the action of a conveyor belt to obtain the final reduced powder. The billet was pressed by cold isostatic pressing technique at 200 MPa pressure, and then the billet was placed in a hydrogen sintering furnace for high-temperature sintering treatment at a sintering temperature of 2573 K with a sintering time of 6 h. The sintered block obtained was hot rolled at a temperature of 1853 K. The W–Y_2O_3 composite material with a rolling rate of 50% was obtained, that is, the thickness of the rolled plate is half of that of the blank. The grain size of W–Y_2O_3 material was 33 ± 25 μm, which was reported in our previous research with the same materials [14].

SEM images and corresponding energy dispersive spectrometer (EDS) mapping of W–Y_2O_3 materials and particle size distribution of Y_2O_3 particles are shown in figure 1. Red arrows indicate some of the Y_2O_3 particles. From the low magnification SEM image, it was found that the particles were uniformly dispersed in the tungsten matrix and the average particle size of the particles was (3.57 ± 1.36) μm. In this work, the standard deviation was used as errors of mean value instead of standard error to reflect the size distribution, this error bar does not directly reflect the confidence interval of the mean value. SEM image shows that the particles tightly bond with the W matrix, and they are identified as Y_2O_3 by EDS (figure 1(*d*)).

2.2. Plasma exposure

Plasma exposure was carried out using a Plasma-Surface Interaction system under Extreme Conditions at Hefei University of Technology, Hefei, China. The sequential

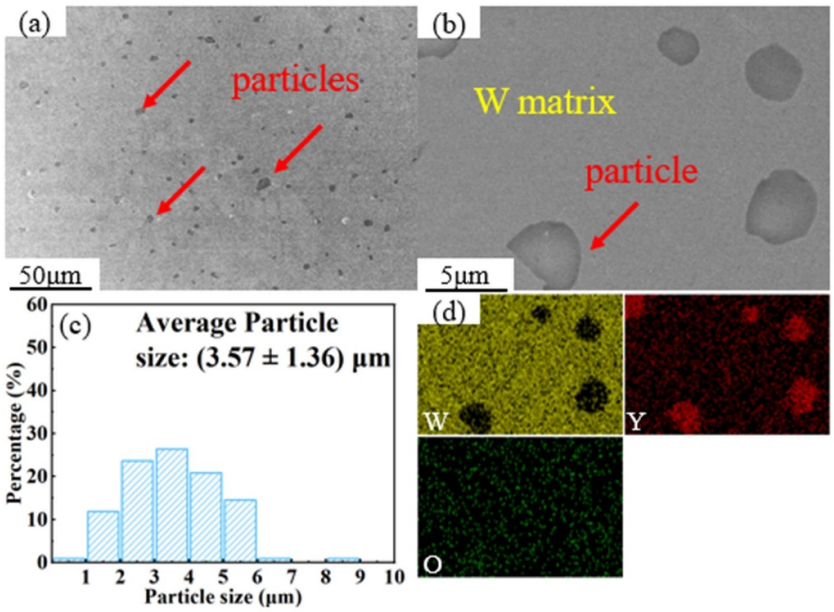


Figure 1. SEM images and corresponding EDS mapping of W–Y_2O_3 materials and particle size distribution of Y_2O_3 particles. (*a*) Low magnification SEM image, (*b*) high magnification SEM image, (*c*) particle size distribution, (*d*) EDS mapping.

Table 1. The detailed parameters of plasma exposure for W–Y_2O_3 materials.

	Specimen number	Flux, Γ_i (10^{21} $m^{-2}\cdot s^{-2}$)	Dose, Θ (10^{24} m^{-2})	Energy, E_i (eV)	Power, P (W)	Temperature[a] (K)
Single D	1	4.0	10.0	50	600	750
	2	6.0	20.0	40	800	830
	3	8.0	50.0	40	1100	950
	4	9.0	100.0	55	1200	1140
Single He	5	7.0	10.0	50	800	850
	6	9.0	50.0	40	1100	960
	7	12.0	100.0	40	1200	1150
Sequential He/D	8	3.0/3.0	2.5/2.5	30/20	500/600	700
	9	5.0/3.5	5.0/5.0	30/25	800/750	800
	10	10.0/8.0	25.0/25.0	60/20	900/1000	920
	11	12.0/9.0	50.0/50.0	70/30	1000/1200	1130
Sequential D/He	12	3.0/3.0	2.5/2.5	20/30	600/500	700
	13	3.5/5.0	5.0/5.0	25/30	750/800	800
	14	8.0/10.0	25.0/25.0	20/60	1000/900	910
	15	9.0/12.0	50.0/50.0	30/70	1200/1000	1120

[a] The average temperature measured using thermocouple behind the sample.

plasma exposure of deuterium and helium, as well as single deuterium and helium, were applied. For convenience, the two sequential plasma exposures of helium followed by deuterium injection and deuterium followed by helium injection are abbreviated as He/D and D/He in this paper. Samples for plasma exposure were mechanically cut into 10 mm × 5 mm × 1 mm. Then, electrolytic polishing is carried out after mechanical polishing, using 0.5 wt.% NaOH aqueous solution as electrolyte. High pure (>99.999%) D and He were used with a gas flow rate of 60 sccm. The vacuum was lower than 3×10^{-4} Pa during plasma exposure. The detailed exposure parameters are listed as table 1. Where the incident ion energy (E_i) is derived from the difference between the plasma space potential (V_s) and the negative bias voltage (V_b), i.e. $E_i = e(V_s - V_b)$.

2.3. Characterization

The microstructure evolution of W–Y_2O_3 material was characterized using Hitachi SU-8020 SEM operated at 5 kV and FEI Tecanai G2 F20 TEM operated at 200 kV. Samples for TEM analysis were prepared using a Helios G4 UX Dual Beam focused ion beam (FIB) system with a Lift-Out model. The

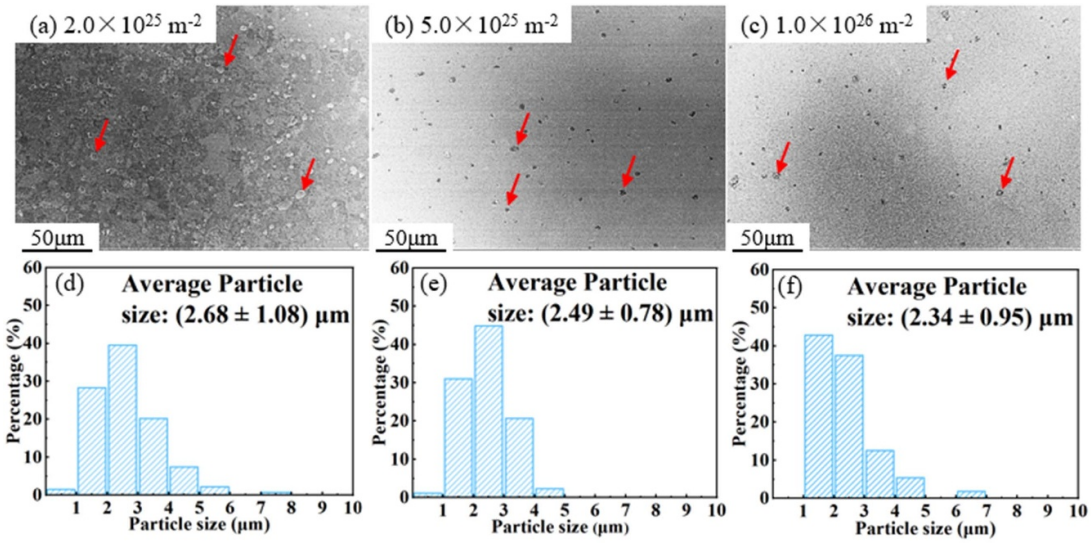


Figure 2. Low magnification SEM images and Y_2O_3 particle size distribution of W–Y_2O_3 material after D plasma exposure with different doses. (*a*), (*d*) 2.0 × 10^{25} D·m^{-2}, (*b*), (*e*) 5.0 × 10^{25} D·m^{-2}, (*c*), (*f*) 1.0 × 10^{26} D·m^{-2}.

Table 2. The detailed results of particle size distribution in W–Y_2O_3 materials after exposure.

Exposure	Dose, Θ (10^{24} m^{-2})	Measured particle number	Particle size (μm)	Standard deviation (μm)	Particle density (10^9 m^{-2})
Non	0	110	3.57	1.36	2.44
Single D	20	134	2.68	1.08	2.98
	50	87	2.49	0.78	1.93
	100	56	2.34	0.95	1.24
Single He	10	100	2.62	1.00	2.22
	50	54	1.97	0.52	1.20
Sequential He/D	10	73	2.67	0.78	1.62
	50	72	2.62	0.65	1.60
	100	54	2.81	0.80	1.20
Sequential D/He	10	110	2.63	1.17	2.44
	50	72	2.07	0.70	1.60
	100	46	2.34	0.61	1.02

element distribution was analyzed using an EDS. The cross-sectional specimens were prepared using the Crossbeam 350 FIB system.

3. Results

3.1. The stability of Y_2O_3 particle

3.1.1. D plasma exposure. Figure 2 shows the low magnification SEM images and Y_2O_3 particle size distribution of W–Y_2O_3 material after D plasma exposure with different doses. These results show that the average size of Y_2O_3 particle was slightly decreased with an increase in dose. Specifically, the mean particle size was measured (2.68 ± 1.08) μm at a dose of 2.0 × 10^{25} D·m^{-2}, which subsequently decreased to (2.49 ± 0.78) μm at a dose of 5.0 × 10^{25} D·m^{-2}. The mean particle size decreased to (2.34 ± 0.95) μm at a dose of 1.0 × 10^{26} D·m^{-2}. The detailed results of particle size distribution in W–Y_2O_3 materials after exposure are listed in table 2, in which the particle density is estimated as a number of particles per unit area, since the observation depth of SEM is limited to the 10 nm level.

High magnification SEM images of Y_2O_3 particle and corresponding EDS mapping of W–Y_2O_3 material after D plasma exposure with different doses were shown in figure 3. At the dose of 2.0 × 10^{25} D·m^{-2}, only a small number of holes were observed on the surface of Y_2O_3 particle. With the dose increasing, the surface of the particles gradually breaks, and the particles seem to be etched and stripped out of the matrix. These results show a larger damage of Y_2O_3 particles rather than the W matrix with the dose increases. There are

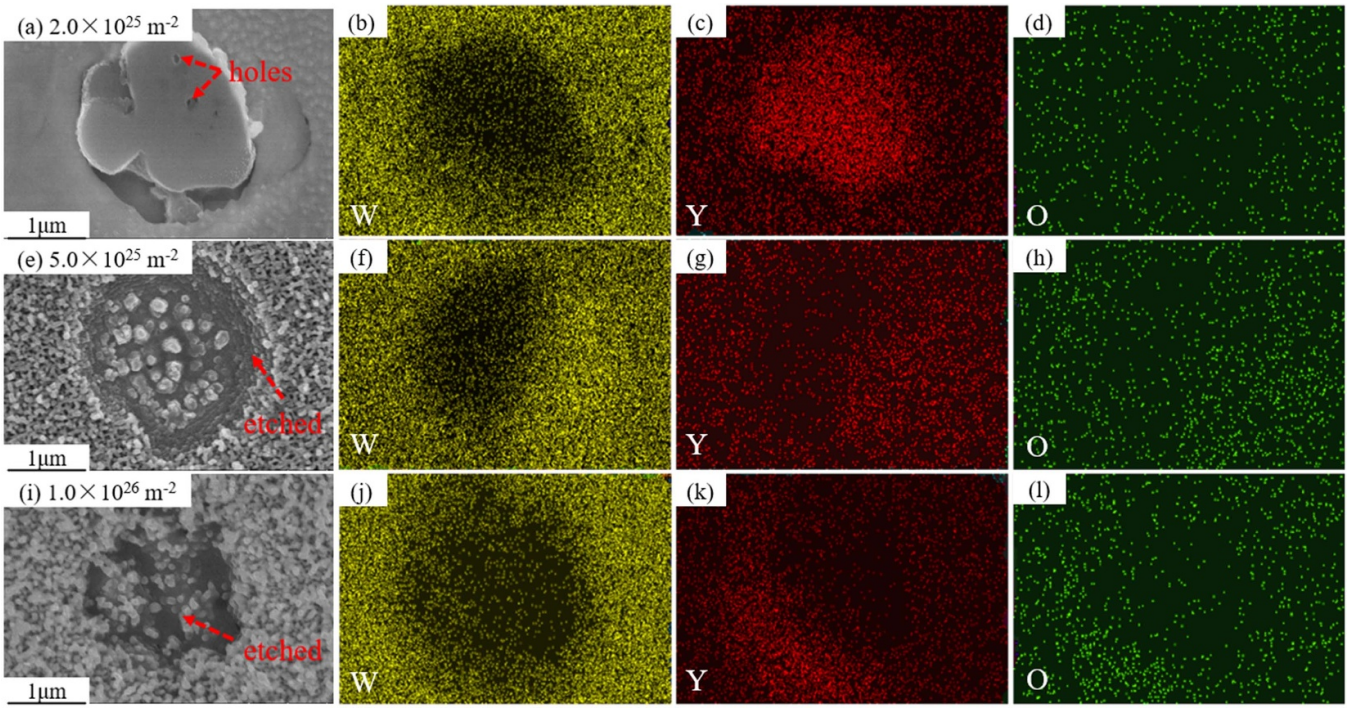


Figure 3. High magnification SEM images of Y_2O_3 particle and corresponding EDS mapping of W–Y_2O_3 material after D plasma exposure with different doses. (*a*)–(*d*) 2.0 × 10^{25} D·m^{-2}, (*e*)–(*h*) 5.0 × 10^{25} D·m^{-2}, (*i*)–(*l*) 1.0 × 10^{26} D·m^{-2}.

two possible reasons for this phenomenon: the one is that Y_2O_3 is directly etched by D plasma [15], as shown in figure 3(*a*), and holes caused by etching were observed on the surface of the particles at low doses. Considering that the sputtering thresholds of Y and O in Y_2O_3 particles are 23 eV and 14 eV [16], respectively, both of which are significantly lower than that of W (about 160 eV [17]), it is reasonable to expect that Y_2O_3 particles would be sputtered before W matrix. The other one is that D atoms are tracked and aggregated at the interface, leading to a higher internal stress, resulting in the cracking and detaching of particles [15, 18]. For example, as shown in figures 3(*e*) and (*i*), interweaved nanotendrils (also called fuzz) morphology of Y_2O_3 particles were observed under high-dose plasma exposure.

3.1.2. He plasma exposure. Figure 4 shows the low magnification SEM images and Y_2O_3 particle size distribution of W–Y_2O_3 material after He plasma exposure with different doses. The results indicate a similarity to D plasma, in which the average size of Y_2O_3 particles decreased as the dose increased. The difference is that the reduction rate of particles under He plasma exposure was significantly enhanced compared to that of D. At the dose of 1.0 × 10^{25} He·m^{-2}, the mean particle size was (2.62 ± 1.00) μm, and it significantly reduced to (1.97 ± 0.52) μm at 5.0 × 10^{25} He·m^{-2}. When the dose reached 1.0 × 10^{26} He·m^{-2}, Y_2O_3 particles cannot be confirmed via SEM image, as shown in figure 4(*c*). Thus, no particle size distribution was obtained at this exposure dose.

High magnification SEM images of Y_2O_3 particle and corresponding EDS mapping of W–Y_2O_3 material after He plasma exposure with different doses were shown in figure 5. At 1 × 10^{25} He·m^{-2}, the result is very similar to that after low dose D plasma exposure, only a small number of holes were observed in Y_2O_3 particle. However, after He plasma exposure at higher doses, the damage of Y_2O_3 particles is significantly greater than that of D plasma. The reason for this phenomenon may be the much lower solubility of He compared to that of D, which significantly increased the internal stress generated by He aggregation. Besides, the aggregation of He at grain boundaries reduces the bond strength and leads to the ejection of W grains [19]. This mechanism may accelerate the spalling process of particles from the matrix. Yao *et al* [20] studied the effects of helium ion irradiation on the damage behavior of W–Y_2O_3 composites following laser thermal shock. They observed the spalling of Y_2O_3 particles in the near-surface region through TEM observation. This spalling is believed to be caused by cracking between the Y_2O_3 particles as a result of the laser thermal shock, which leads to the shedding of Y_2O_3 grains in that region. Considering that the plasma beam in this study also imposes a large thermal load and thermal stress, it may lead to some grain ejection or spalling, similar to W grain ejection, as shown in figure 5(*e*). However, since this experiment maintains a uniform temperature rather than a thermal shock temperature, this mechanism is not predominant.

The TEM images of the Y_2O_3/matrix interface and corresponding selected area electron diffraction (SAED) patterns were shown in figure 6. The labeled sites C and D in figure 6(*b*)

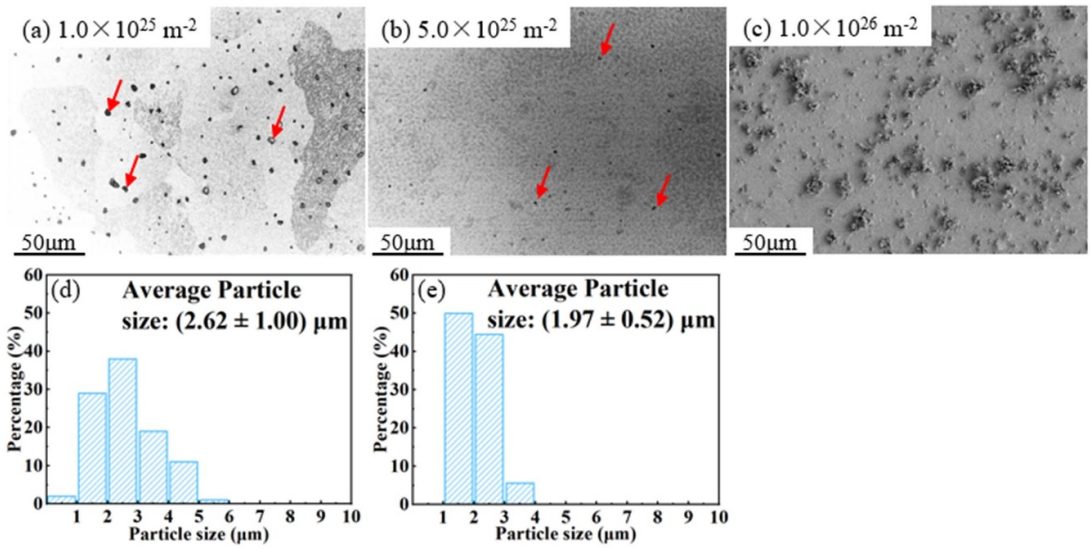


Figure 4. Low magnification SEM images and Y_2O_3 particle size distribution of W–Y_2O_3 material after He plasma exposure with different doses. (*a*), (*d*) 1 × 10^{25} He·m^{-2}, (*b*), (*e*) 5.0 × 10^{25} He·m^{-2}, (*c*) 1.0 × 10^{26} He·m^{-2}.

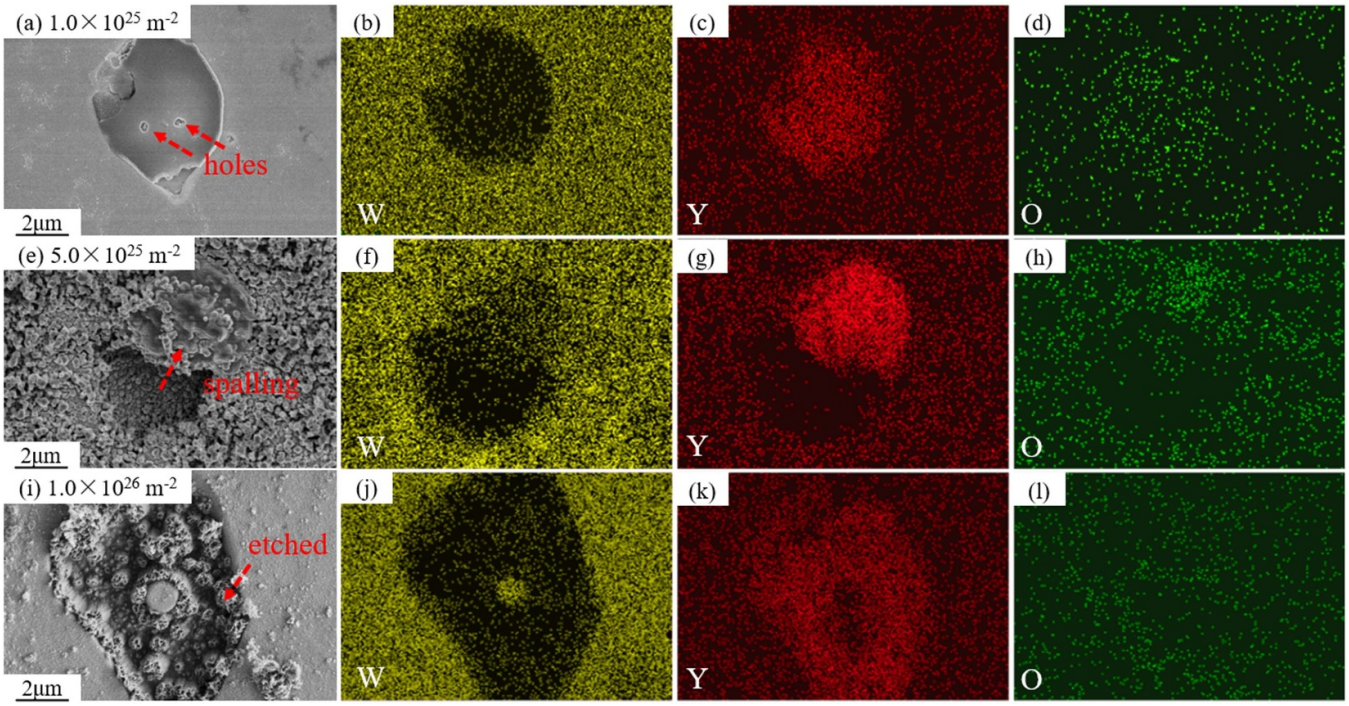


Figure 5. High magnification SEM images of Y_2O_3 particle and corresponding EDS mapping of W–Y_2O_3 material after He plasma exposure with different doses. (*a*)–(*d*) 1 × 10^{25} He·m^{-2}, (*e*)–(*h*) 5.0 × 10^{25} He·m^{-2}, (*i*)–(*l*) 1.0 × 10^{26} He·m^{-2}.

are identified by the SAEDs in figures 6(*c*) and (*d*), respectively. The Y_2O_3/matrix interface was confirmed via SAED results. Figure 6(*b*) shows a significant void and small broken particles at the interface, suggesting that the destruction of particles begins at the interface. Besides, some bubbles were observed near the void (as shown in figure 6(*a*)), showing that the destruction of particles is highly correlated with the generation and aggregation of bubbles.

3.1.3. Sequential He/D plasma exposure. Low magnification SEM images and Y_2O_3 particle size distribution of W–Y_2O_3 material after sequential He/D plasma exposure with different doses were shown in figure 7. Interestingly, a significant decrease in the number of particles was observed in the SEM images, but no particle size reduction was observed. The mean particle size with a dose of 5 × 10^{24} He·m^{-2} + 5 × 10^{24} D·m^{-2} was

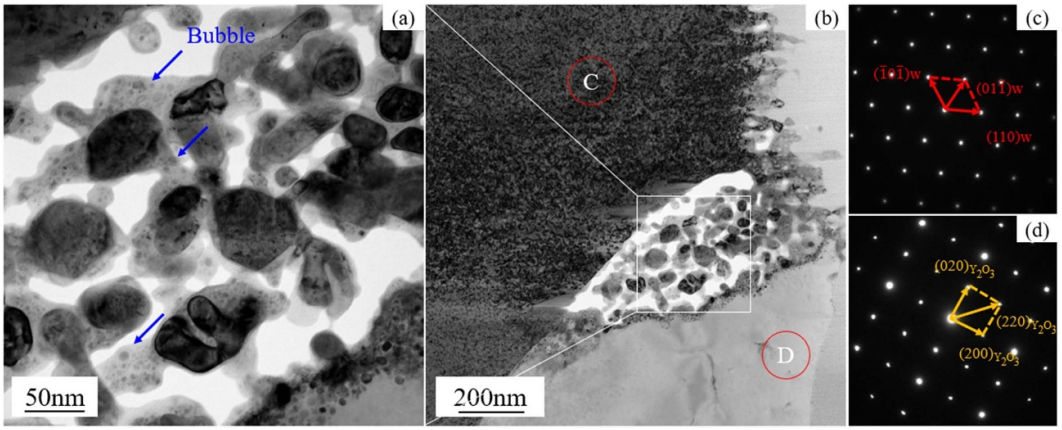


Figure 6. The TEM images of the Y_2O_3/matrix interface and corresponding SAED patterns. (*a*), (*b*) A is the enlarged TEM image at the position of the white box in figure (*b*); (*c*), (*d*) are the SAED patterns of the C and D phases in figure (*b*), respectively.

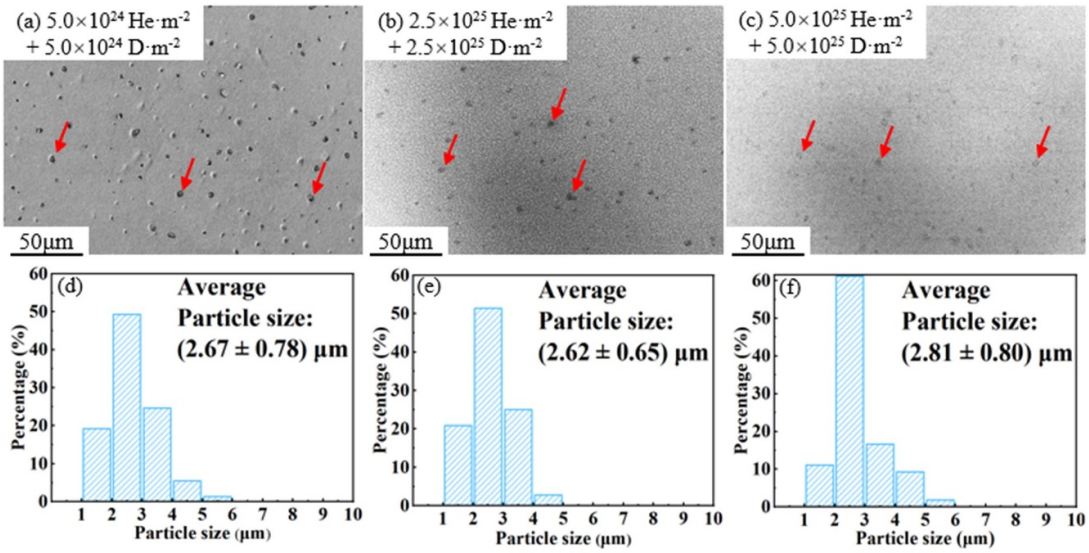


Figure 7. Low magnification SEM images and Y_2O_3 particle size distribution of W–Y_2O_3 material after sequential He/D plasma exposure with different doses. (*a*), (*d*) 5×10^{24} He·m^{-2} + 5×10^{24} D·m^{-2}, (*b*), (*e*) 2.5×10^{25} He·m^{-2} + 2.5×10^{25} D·m^{-2}, (*c*), (*f*) 5.0×10^{25} He·m^{-2} + 5.0×10^{25} D·m^{-2}.

(2.67 ± 0.78) μm, and the mean particle size with a dose of 2.5×10^{25} He·m^{-2} + 2.5×10^{25} D·m^{-2} was (2.62 ± 0.65) μm, which was almost the same. When the dose reached 5.0×10^{25} He·m^{-2} + 5.0×10^{25} D·m^{-2}, the mean particle size slightly changed to (2.81 ± 0.80) μm. Considering the decrease in particle density and the fuzz structure on the W matrix extending through the interface to the particle surface, which leads to the blurring of the particle morphology, this difference may be due to the increase in measurement error. Especially, in figure 7(*c*), small particles are almost unobservable, and it will also lead to a larger average particle size. Based on the above analysis, it is reasonable that the particle size is considered as slight decrease or almost unchanged during the sequential He/D plasma exposure.

High magnification SEM images of Y_2O_3 particle and corresponding EDS mapping of W–Y_2O_3 material after sequential He/D plasma exposure with different doses were shown in figure 8. At the dose of 5.0×10^{24} He·m^{-2} + 5.0×10^{24} D·m^{-2}, the W–Y_2O_3 interface exhibits cracking, but no holes or broken area were observed at the surface of Y_2O_3 particle. When the dose reached 2.5×10^{25} He·m^{-2} + 2.5×10^{25} D·m^{-2}, some holes were observed at the surface of the Y_2O_3 particle, and crack propagation was observed at the interface. Besides, some fuzz structure appears at the W and Y_2O_3 surface. At a higher dose (5.0×10^{25} He·m^{-2} + 5.0×10^{25} D·m^{-2}), the fuzz structure further developed, and the interface became blurred. This may be why a larger mean particle size was measured in figures 7(*c*) and (*f*). In figure 8(*b*), it seems some W signal is

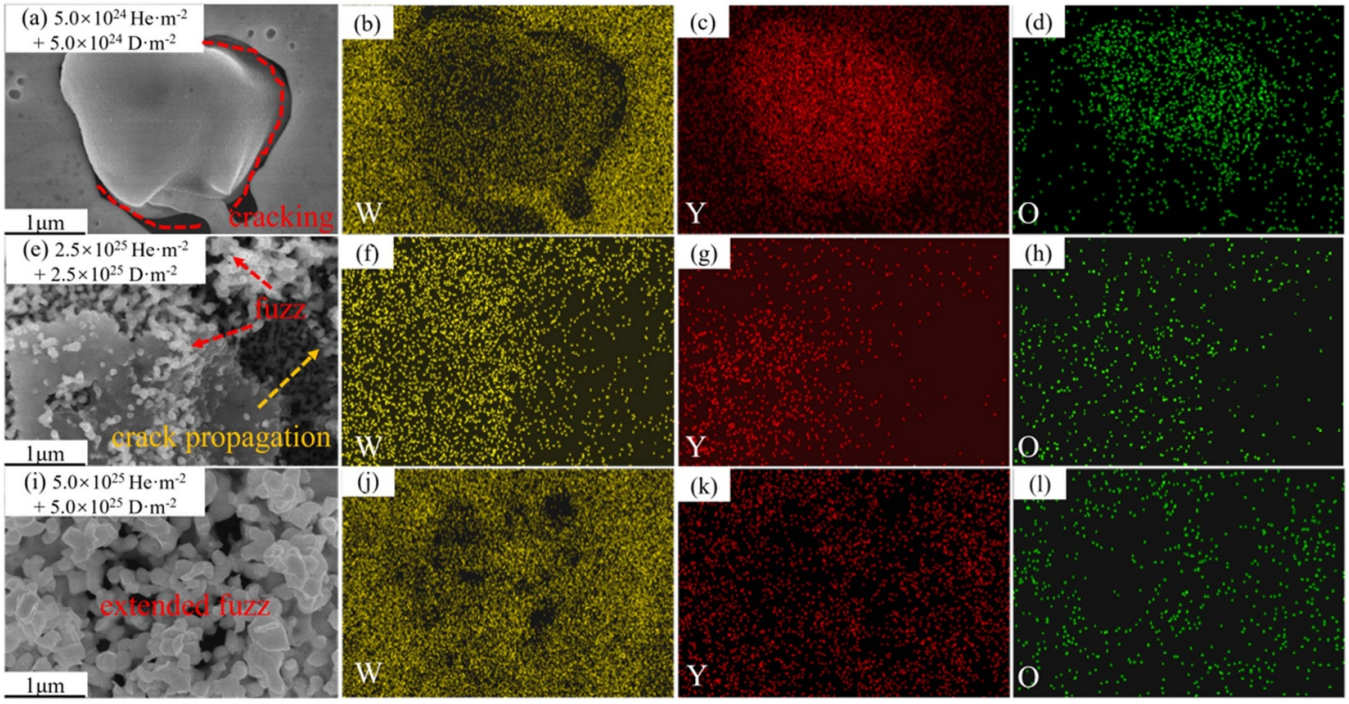


Figure 8. High magnification SEM images of Y_2O_3 particle and corresponding EDS mapping of W–Y_2O_3 material after sequential He/D plasma exposure with different dose. (*a*)–(*d*) 5.0×10^{24} He·m^{-2} + 5.0×10^{24} D·m^{-2}, (*e*)–(*h*) 2.5×10^{25} He·m^{-2} + 2.5×10^{25} D·m^{-2}, (*i*)–(*l*) 5.0×10^{25} He·m^{-2} + 5.0×10^{25} D·m^{-2}.

observed in the particles, which may be due to the sputtering of W onto Y_2O_3 particles. However, it should be noted that the detection depth of EDS is higher than 1 μm, suggesting that these signals may also be caused by the W at the bottom of the particles. This issue will be further analyzed using cross-sectional samples in section 3.3. Besides, in figure 8(*e*), we can observe sparse W clusters deposited on the Y_2O_3 particle, which are likely formed due to subthreshold sputtering of Guseva *et al* [21] proposed that the subthreshold sputtering is attributed to the possible sputtering of W adsorbed atoms. The energy required to dislodge the adsorbed atoms from the surface by helium ion bombardment is approximately one-third of the physical sputtering threshold [22]. Considering that the physical sputtering threshold for W is over 100 eV [23, 24], and the energy of the helium ions used in this study is 60 eV, sub-sputtering is indeed a possible occurrence. The EDS element distribution simultaneously identifies W, Y, and O, which are mixed. In figure 8(*i*), fuzz is observed growing on the W substrate, crossing the phase boundary and extending into the particle region. The extension of this fuzz results in the partial obscuration of the particles. Similarly, Li *et al* [18] also reported a similar phenomenon.

3.1.4. Sequential D/He plasma exposure. Low magnification SEM images and Y_2O_3 particle size distribution of W–Y_2O_3 material after sequential D/He plasma exposure with different doses were shown in figure 9. The results showed a similar trend on the particle size evolution. With the dose of 5.0×10^{24} D·m^{-2} + 5.0×10^{24} He·m^{-2}, the mean particle size was (2.63 ± 1.17) μm, and it decreased to (2.07 ± 0.70) μm at the dose of 2.5×10^{25} D·m^{-2} + 2.5×10^{25} He·m^{-2}. However, the average particle size increases to (2.34 ± 0.61) μm at the dose of 5.0×10^{25} D·m^{-2} + 5.0×10^{25} He·m^{-2}. This may be due to the same reason as described in section 3.1.3, where particles are covered by fuzz, resulting in the invisibility of small particles.

High magnification SEM images of Y_2O_3 particle and corresponding EDS mapping of W–Y_2O_3 material after sequential D/He plasma exposure at different doses were shown in figure 10. As shown in figure 10(a), an obvious fuzz structure was observed at the W matrix and near the interface. Y_2O_3 particles were quickly covered by fuzz with increasing doses. Obviously, the development of fuzz structures and the damage to particles during D/He plasma exposure is more rapid than that during He/D plasma exposure. The formation of fuzz is mainly related to the evolution of bubbles as well as the interaction between D/He and defects such as vacancies [25]. This phenomenon implies a significant synergistic effect between D/He during plasma exposure.

3.2. The evolution of W–Y_2O_3 surface morphology

3.2.1. D plasma exposure. Besides the damage of Y_2O_3 particles, the damage of the W matrix was observed in all samples. Figure 11 shows the surface morphology of W–Y_2O_3 material after D plasma exposure with different doses, where figures 11(*a*)–(*c*) show the low-magnification morphology and figures 11(*d*)–(*f*) show the corresponding high-magnification image. At the dose of 1.5×10^{25} D·m^{-2}, it is not difficult to find typical stepped D blister from figure 11(a), which can

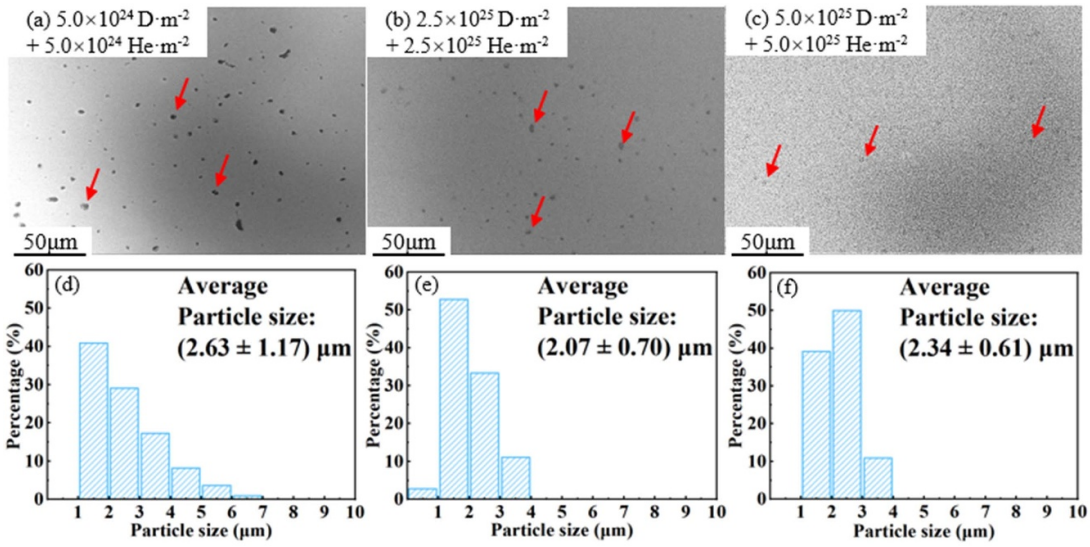


Figure 9. Low magnification SEM images and Y_2O_3 particle size distribution of W–Y_2O_3 material after sequential D/He plasma exposure with different doses. (*a*), (*d*) 5.0 × 10^{24} D·m^{-2} + 5.0 × 10^{24} He·m^{-2}, (*b*), (*e*) 2.5 × 10^{25} D·m^{-2} + 2.5 × 10^{25} He·m^{-2}, (*c*), (*f*) 5.0 × 10^{25} D·m^{-2} + 5.0 × 10^{25} He·m^{-2}.

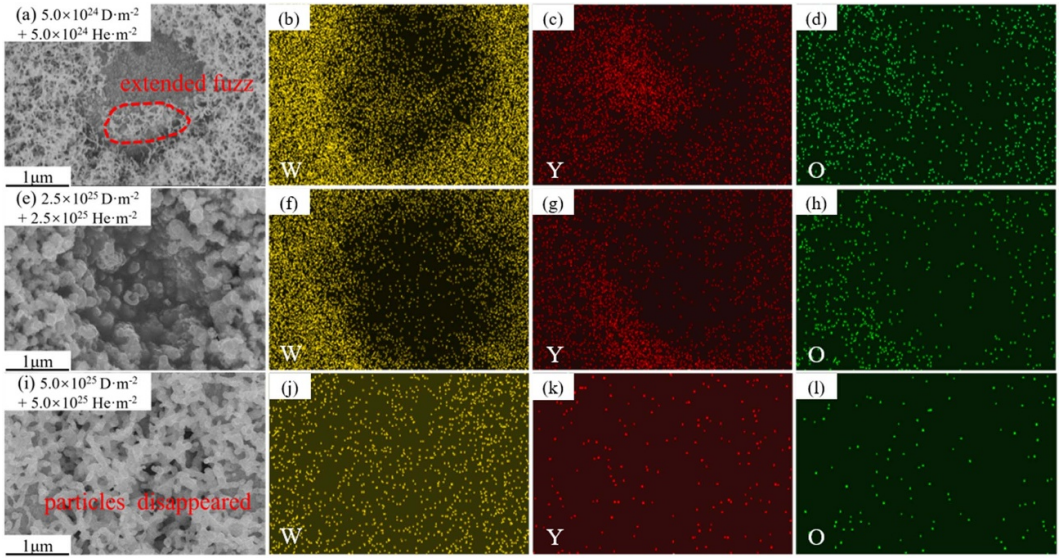


Figure 10. High magnification SEM images of Y_2O_3 particle and corresponding EDS mapping of W–Y_2O_3 material after sequential D/He plasma exposure with different doses. (*a*)–(*d*) 5.0 × 10^{24} D·m^{-2} + 5.0 × 10^{24} He·m^{-2}, (*e*)–(*h*) 2.5 × 10^{25} D·m^{-2} + 2.5 × 10^{25} He·m^{-2}, (*i*)–(*l*) 5.0 × 10^{25} D·m^{-2} + 5.0 × 10^{25} He·m^{-2}.

be attributed to the lateral stress [26]. When the concentration of D atoms reaches supersaturation, the lateral stress induced by supersaturated D atoms results in local cracking of the W matrix [27]. At the same time, the dislocations start to slip to release the stress. Note that the most common slip systems for BCC metals are [111]{110}, thus, dislocations may slide along the [111] direction at {110} crystal plane, leading to the appearance of stepped D bubbles [28]. Figure 11(*d*) shows the high magnification image at the dose of 1.5 × 10^{25} D·m^{-2}, cone-shaped and wavy were observed at positions A and B, respectively. This phenomenon indicated that the damage of tungsten is affected by crystallographic orientation [29]. When the dose reached 5.0 × 10^{25} D·m^{-2}, nano-like fluffy structures (fuzz) were observed, and it was further evolved into coarser at a dose of 1.0 × 10^{26} D·m^{-2}.

3.2.2. He plasma exposure. The surface morphology of W–Y_2O_3 material under different He plasma irradiation was shown in figure 12. As shown in figure 12(a), morphology was different from that of the H plasma exposure sample, with an obvious fuzzy surface being observed. This phenomenon indicates that He causes much greater damage to the W matrix than D, which may be due to the lower solubility of He in W. With the dose increasing, some coral-like morphology was observed. For example, figure 12(e) shows the combination

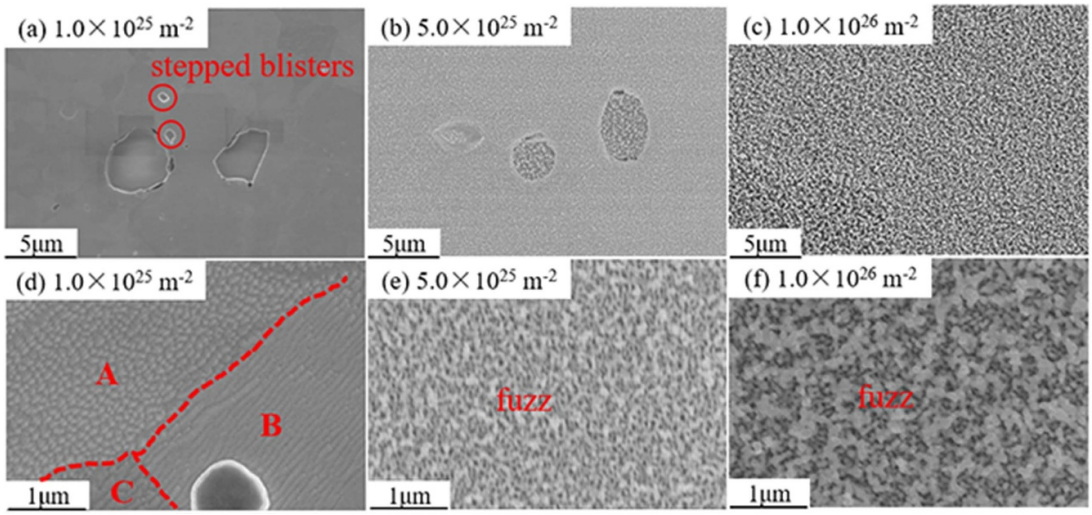


Figure 11. SEM images of W–Y_2O_3 at different doses of D plasma exposure. (*a*)–(*c*) Low magnification SEM images, (*d*)–(*f*) high magnification SEM images. (*a*), (*d*) 1.0 × 10^{25} D·m^{-2}, (*b*), (*e*) 5.0 × 10^{25} D·m^{-2},(*c*), (*f*) 1.0 × 10^{26} D·m^{-2}.

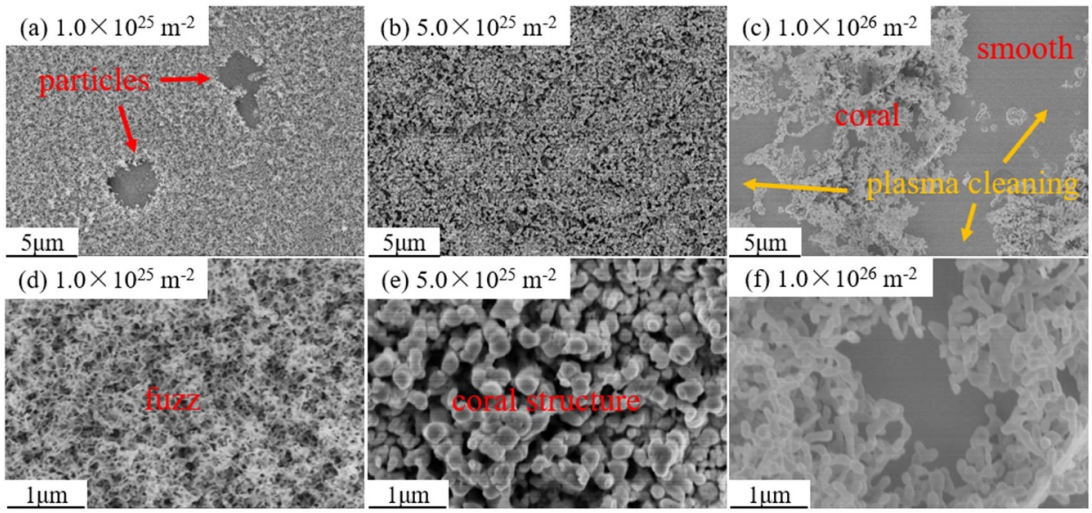


Figure 12. SEM images of W–Y_2O_3 at different doses of He plasma exposure. (*a*)–(*c*) Low-magnification SEM images, (*d*)–(*f*) high-magnification SEM images. (*a*), (*d*) 1.0 × 10^{25} He·m^{-2},(*b*), (*e*) 5.0 × 10^{25} He·m^{-2},(*c*), (*f*) 1.0 × 10^{26} He·m^{-2}.

of fuzz and holes at the surface of W matrix with a dose of 5.0 × 10^{25} He m^{-2}. Interestingly, when the dose reaches 1.0 × 10^{26} He m^{-2}, the surface has only localized coral structures, which have been partially detached, and the detached substrate surface becomes smooth again. It seems like some kind of the plasma cleaning [30].

3.2.3. Sequential He/D plasma exposure. The surface morphology of W–Y_2O_3 material under different He/D plasma exposures is shown in figure 13. With a dose of 2.5 × 10^{24} He·m^{-2} + 2.5 × 10^{24} D·m^{-2}, only a large number of high-density spherical structures (white granular dots) with a rough surface can be found as shown in figure 13(*a*). High magnification image shows a combination of spherical and pinhole-like. With increasing doses, the conjugate evolves into larger pores, which is attributed to the large number of aggregated nanoscale He vesicles under the near-surface layer. When the dose increased to 2.5 × 10^{25} He·m^{-2} + 2.5 × 10^{25} D·m^{-2}, the fuzz structure appeared. At a dose of 5.0 × 10^{25} He·m^{-2} + 5.0 × 10^{25} D·m^{-2}, the surface shows a three-dimensional labyrinthine fuzz structure and the fuzz is distributed with bubbles, which is closely related to the already formed fuzz structure described above.

3.2.4. Sequential D/He plasma exposure. Figure 14 shows the surface morphology of W–Y_2O_3 material under different doses of D/He plasma exposure. At the dose of 2.5 × 10^{24} D·m^{-2} + 2.5 × 10^{24} He·m^{-2}, the hill-like pores and fibrous bonding can be clearly observed in

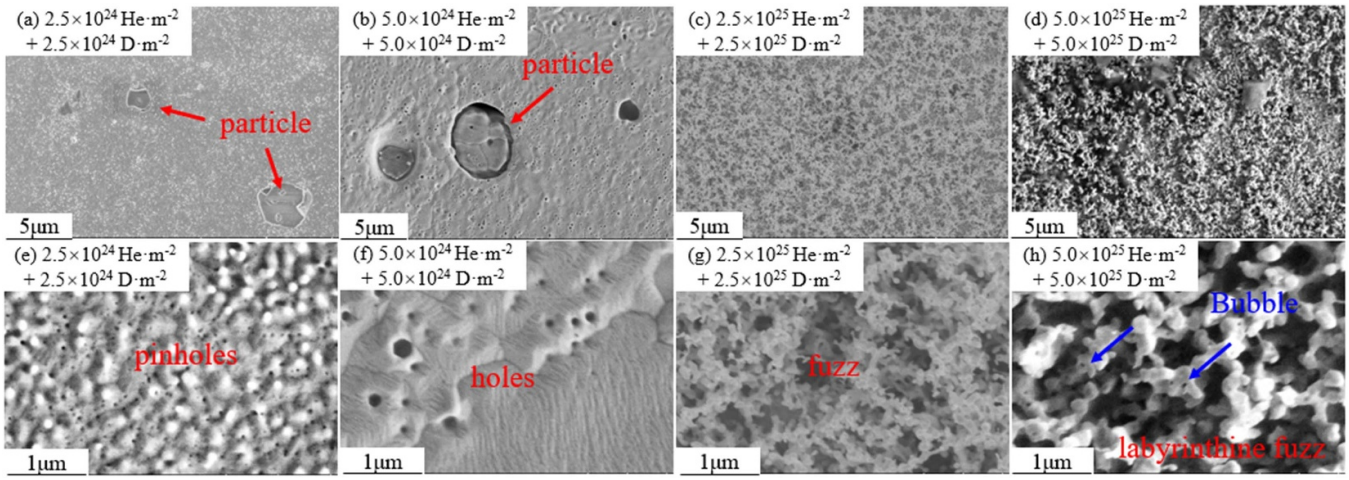


Figure 13. SEM images of W–Y_2O_3 at different doses of He/D plasma exposure. (a)–(d) Low-magnification SEM images, (e)–(h) high-magnification SEM images. (*a*), (*e*) 2.5 × 10^{24} He·m^{-2} + 2.5 × 10^{24} D·m^{-2}, (*b*), (*f*) 5.0 × 10^{24} He·m^{-2} + 5.0 × 10^{24} D·m^{-2}, (*c*), (*g*) 2.5 × 10^{25} He·m^{-2} + 2.5 × 10^{25} D·m^{-2}, (*d*), (*h*) 5.0 × 10^{25} He·m^{-2} + 5.0 × 10^{25} D·m^{-2}.

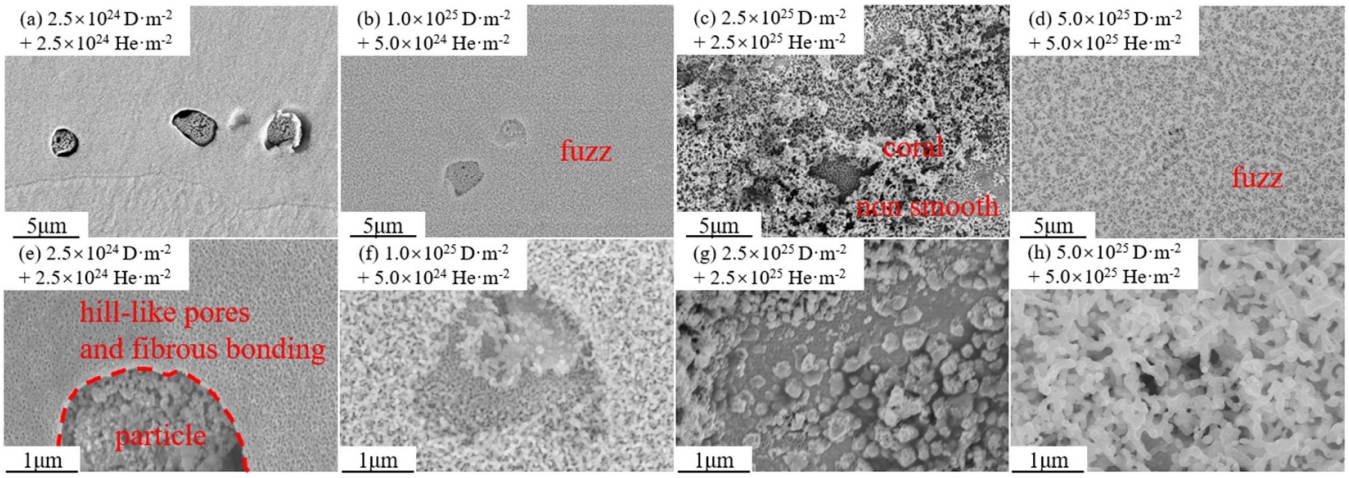


Figure 14. SEM images of W–Y_2O_3 at different doses of D/He plasma exposures. (*a*)–(*d*) Low-magnification SEM images, (*e*)–(*h*) high-magnification SEM images. (*a*), (*e*) 2.5 × 10^{24} D·m^{-2} + 2.5 × 10^{24} He·m^{-2}, (*b*), (*f*) 1.0 × 10^{25} D·m^{-2} + 5.0 × 10^{24} He·m^{-2}, (*c*), (*g*) 2.5 × 10^{25} D·m^{-2} + 2.5 × 10^{25} He·m^{-2}, (*d*), (*h*) 5.0 × 10^{25} D·m^{-2} + 5.0 × 10^{25} He·m^{-2}.

figure 14(*e*). As described in section 3.1.4, the D/He irradiation causes more damage than He/D. With a dose of 1.0 × 10^{25} D·m^{-2} + 1.0 × 10^{25} He·m^{-2}, the familiar fuzz structure was observed as shown in figure 14(*f*). When the dose reaches 2.5 × 10^{25} D·m^{-2} + 2.5 × 10^{25} He·m^{-2}, the local region of fuzz is stacked densely, the detached fuzz region no longer leaves a smooth morphology (like figure 12(*c*)), but a combination of pores and fibrous structure. When the dose reached 5.0 × 10^{25} D·m^{-2} + 5.0 × 10^{25} He·m^{-2}, the substrate surface re-evolved into a relatively flat labyrinth-type fuzz layer [31].

3.3. The cross-sectional morphology of fuzz structure

Figure 15 shows the cross-sectional SEM images of fuzz structure after exposure to single D or He plasma. At the dose of 1 × 10^{25} D·m^{-2}, the fuzz layer was almost invisible, and the thickness was about 30 nm. When the D plasma dose reached 1.0 × 10^{26} D·m^{-2}, the thickness of the fuzz layer increased to about 400 nm. However, the thickness of the fuzz layer was measured as about 630 nm with a dose of 1 × 10^{25} He·m^{-2}, which is larger than that of D. When the dose increased to 5 × 10^{25} He·m^{-2}, the fuzz developed to over 1 μm and some fuzz peeled off, leaving a thin area. Figure 16 shows the cross-sectional SEM images of the fuzz structure after exposure to sequential He/D or D/He plasma. At the dose of 2.5 × 10^{24} He·m^{-2} + 2.5 × 10^{24} D·m^{-2}, the fuzz layer was about 40 nm, and it developed to 700 nm with a dose of 5 × 10^{25} He·m^{-2} + 5 × 10^{25} D·m^{-2}. In D/He plasma exposure, the initial thickness (at the dose of 2.5 × 10^{24} D·m^{-2} + 2.5 × 10^{24} He·m^{-2}) of the fuzz layer was 150 nm, and it developed to about 750 nm at the dose of 5 × 10^{25} D·m^{-2} + 5 × 10^{25} He·m^{-2}.

It should be noted that the distribution of fuzz is inhomogeneous at high exposure doses. Figure 17 shows the fuzz structure after exposure to He plasma with a dose of

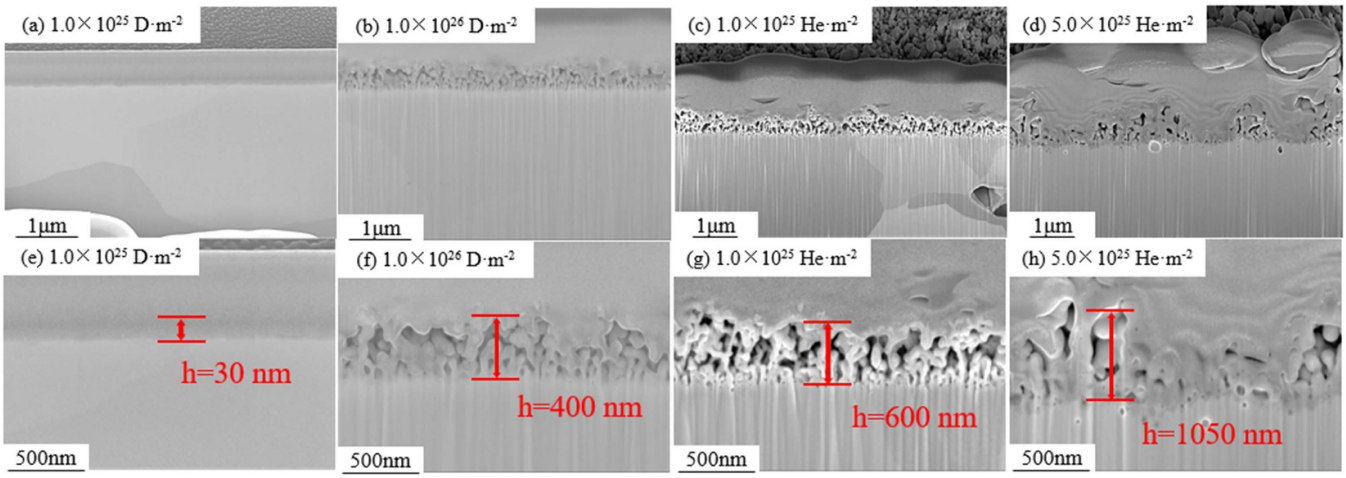


Figure 15. The cross-sectional SEM images of fuzz structure after exposure to single D or He plasma. (*a*), (*e*) 1.0×10^{24} D·m^{-2}, (*b*), (*f*) 1.0×10^{26} D·m^{-2}, (*c*), (*g*) 1.0×10^{25} He·m^{-2}, (*d*), (*h*) 5.0×10^{25} He·m^{-2}.

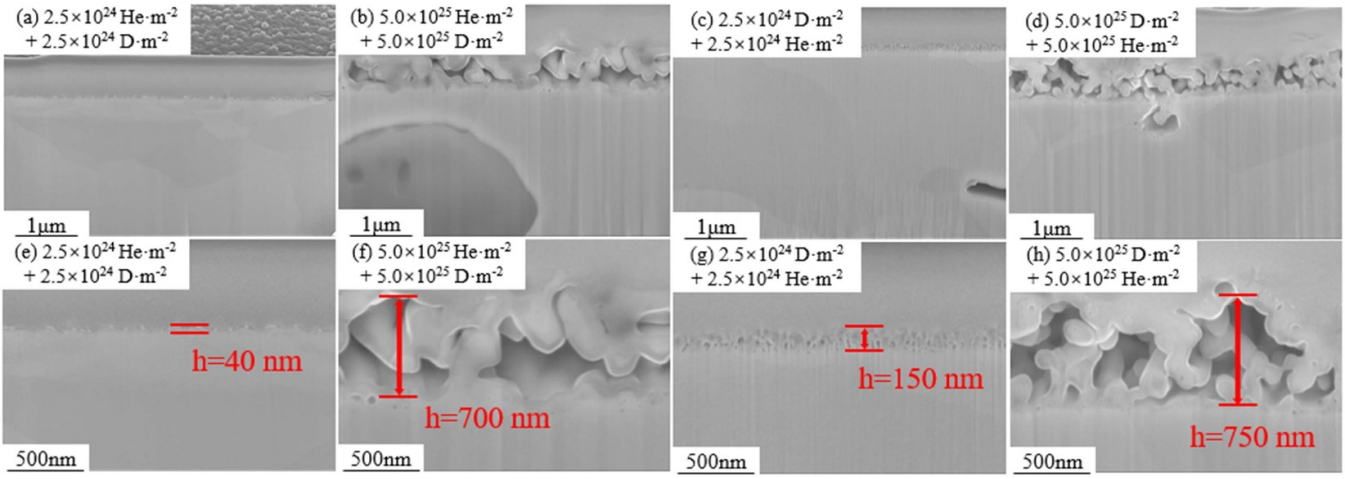


Figure 16. The cross-sectional SEM images of fuzz structure after exposure to sequential He/D or D/He plasma. (*a*), (*e*) 2.5×10^{24} He·m^{-2} + 2.5×10^{24} D·m^{-2}, (*b*), (*f*) 5.0×10^{25} He·m^{-2} + 5.0×10^{25} D·m^{-2}, (*c*), (*g*) 2.5×10^{24} D·m^{-2} + 2.5×10^{24} He·m^{-2}, (*d*), (*h*) 5.0×10^{25} D·m^{-2} + 5.0×10^{25} He·m^{-2}.

1×10^{26} He·m^{-2}. In some areas, very thick fuzz layers (>3 μm) can be observed, while in other areas, the fuzz layer is very thin (<50 nm). This result is similar to figure 12(c), the possible reason is that the surface fuzz is cleaned during plasma exposure.

Figure 18 shows the cross-sectional SEM images of fuzz on Y_2O_3 particles and the corresponding EDS mapping. Figures 18(*a*) and (*e*) show the element distribution after single D plasma exposure with a dose of 1.0×10^{25} D·m^{-2} and 1.0×10^{26} D·m^{-2}, it can be seen that Y_2O_3 particles are etched. This result indicates that Y_2O_3 particles are sputtered faster than the W matrix. However, figures 18(*i*), (*m*), and (*q*) show that the Y_2O_3 particles are covered by fuzz and the fuzz layer on the surface of Y_2O_3 particles is composed of W. A reasonable explanation is that the fuzz on the surface of Y_2O_3 particles is mainly formed by the deposition of W atoms.

4. Discussion

4.1. The evolution of Y_2O_3 particle

It has been widely verified that the addition of Y_2O_3 has a great effect on the mechanical properties of W-based alloy. However, as described above, the average size of Y_2O_3 seems to have decreased, suggesting that Y_2O_3 particles seem to undergo etching or sputtering, which will reduce the particle size. On the other hand, the deposition of W will lead to an 'increase' in particle size, which is not really an increase but only a visual effect. Thus, the evolution of particles can be divided into three different situations: etching-controlled, deposition-controlled and mixed-controlled. Figure 19 shows the average Y_2O_3 particle size as a function of irradiation dose. The Y_2O_3 particle size evolution under D or He plasma exposure shows similar tendencies. The particle size evolution is etching controlled at first, and it changes to mixed

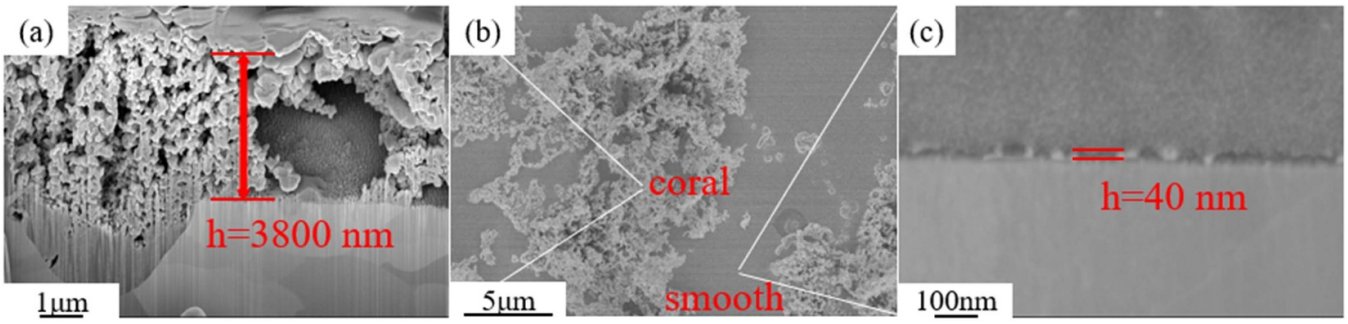


Figure 17. The surface and cross-sectional SEM images of fuzz structures after exposure to single He plasma at a dose of 1.0×10^{26} He·m^{-2}.

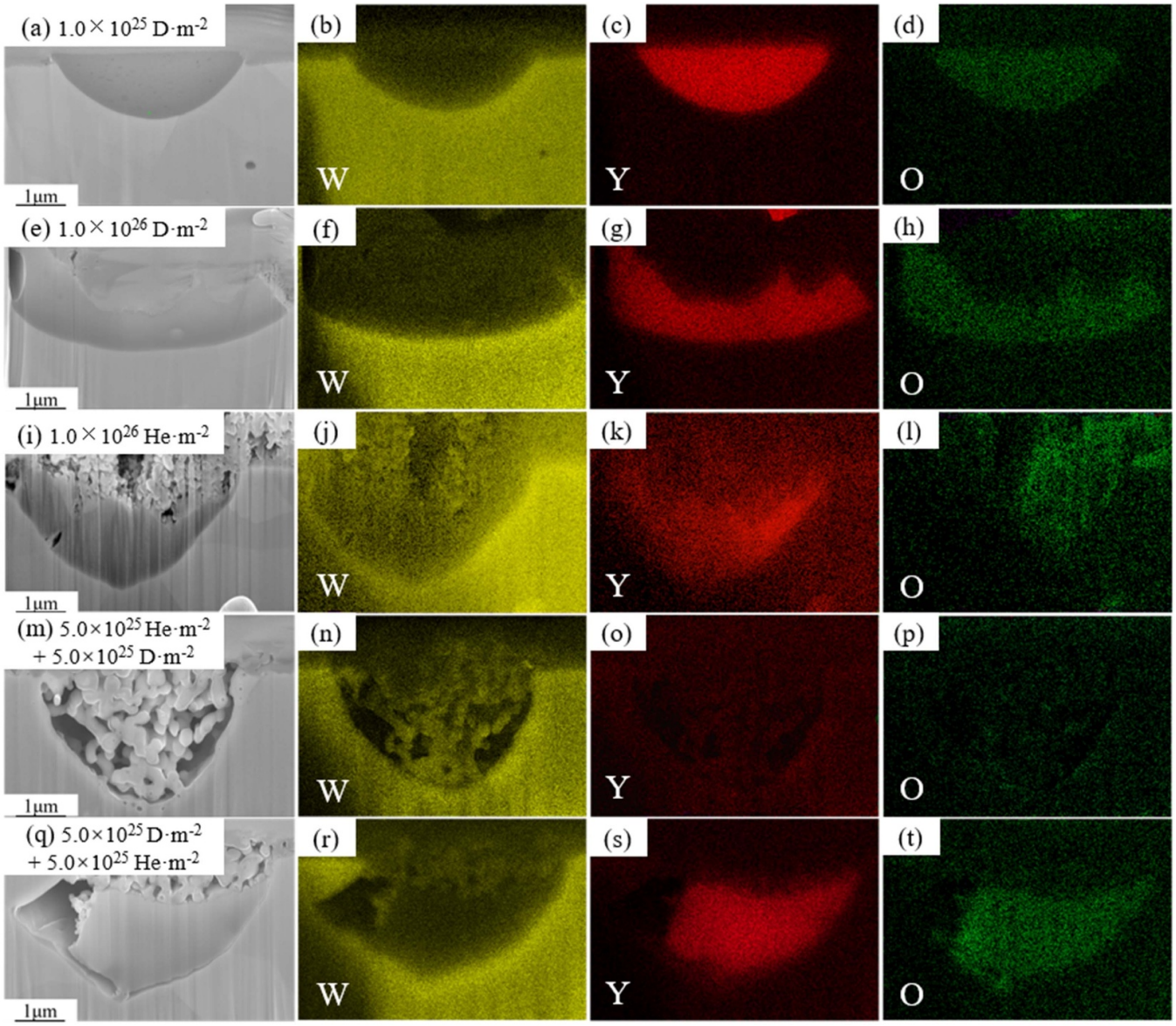


Figure 18. The cross-sectional SEM images of fuzz on Y_2O_3 particles and the corresponding EDS mapping of the W–Y_2O_3 material after single D, He, and sequential He/D, D/He plasma exposure.

controlled with a dose higher than 2×10^{25} m^{-2}. However, the particle evolution under sequential D/He or He/D plasma exposure is different. Both kinds of sequential exposure show an etching-controlled process at first and change to the deposition-controlled process finally. The difference between them is the dose entering the deposition-controlled process. In

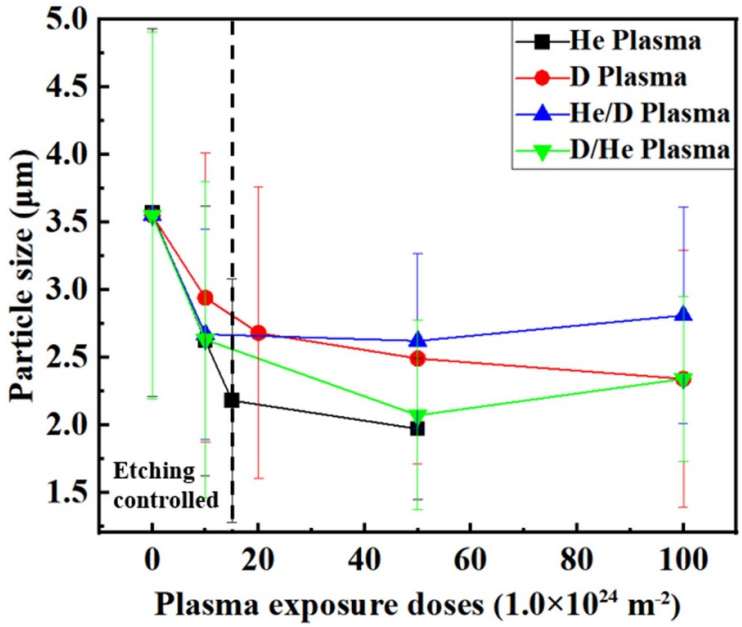


Figure 19. The average Y_2O_3 particle size as a function of plasma exposure doses. The standard deviation was used as error bars.

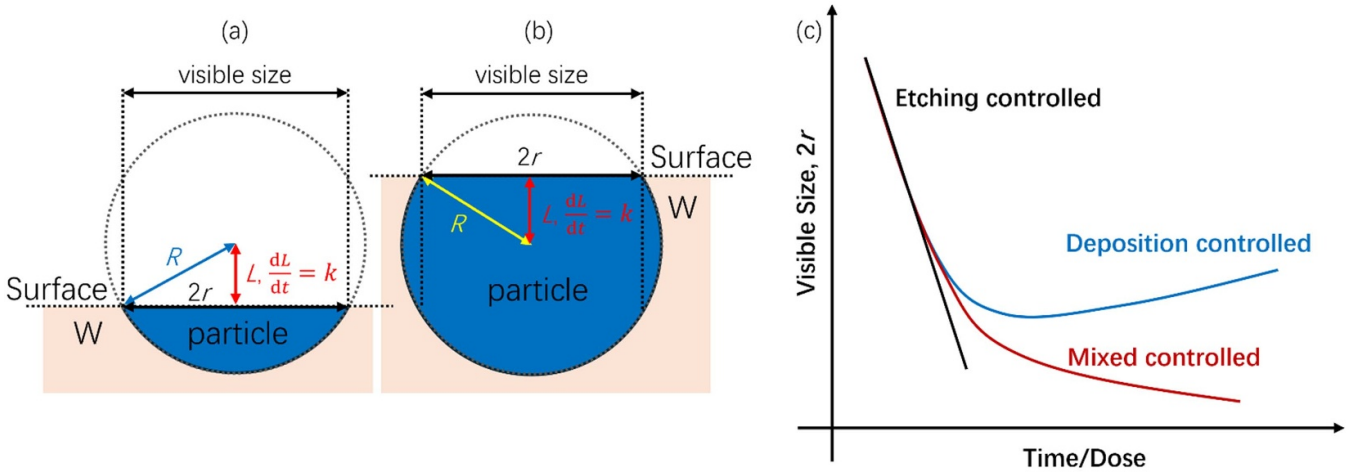


Figure 20. The sketch of particle size evolution in different situations. (*a*) Surface on the lower hemisphere of particle, (*b*) surface on the upper hemisphere of particle, (*c*) visible size evolution.

D/He plasma exposure, the size evolution begins deposition-controlled at a dose of about 5×10^{25} m^{-2}, which is just the end of the etching-controlled stage. In He/D exposure, the etching-controlled stage ended at a dose of 1×10^{25} m^{-2}, and then it changed to mixed-controlled until 5×10^{25} m^{-2}. Finally, the particle size evolution was deposition-controlled, which shows a mean size increase.

Figure 20 shows the sketch of particle size evolution in different situations. Considering that the visible size of particles is the cross-section (surface of sample) of particles, the visible size of particles is dependent on particle shape, as shown in figures 20 (*a*) and (*b*). For an etching-controlled size evolution of a spherical Y_2O_3 particle with a constant etching rate k, if the surface is on the lower hemisphere of it (as shown in figure 20(*a*)), the visible radius r can be estimated based on geometry:

$$\frac{\mathrm{d}r}{\mathrm{d}t} = \frac{Lk}{\sqrt{R^2 - L^2}} \approx \frac{L}{R}k \tag{1}$$

where R is the real particle size. However, if the surface is on the upper hemisphere of the particle (as shown in figure 20(*b*)), the visible size remains unchanged due to the sputter rate of the W matrix being much lower. In the deposition-controlled process, the deposition rate is higher than the etching rate (meaning a negative k). The particle size will grow due to the

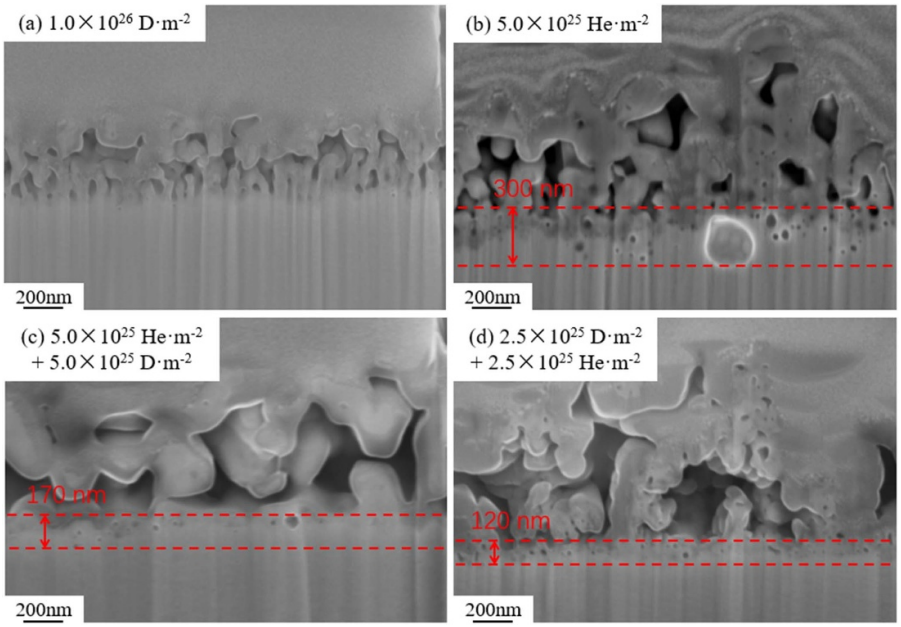


Figure 21. The bubbles in the bottom of the fuzz layer for the samples after exposure to different conditions. (*a*) 1.0×10^{26} D·m^{-2}, (*b*) 5.0×10^{25} He·m^{-2}, (*c*) 5.0×10^{25} He·m^{-2} + 5.0×10^{25} D·m^{-2}, (*d*) 2.5×10^{25} D·m^{-2} + 2.5×10^{25} He·m^{-2}.

deposition of W and finally be covered by fuzz. In the mixed-controlled process, the etching rate was lower but still positive, leading to a lower size reduction.

Thus, the size evolution of Y_2O_3 particles includes three stages: the first stage was etching-controlled, in which the particle size rapidly decreases at a constant rate. The second stage was mixed-controlled, in which the particle size decreased at a gradually decreasing rate caused by the deposition of W atoms. The third stage was deposition-controlled. In this stage, the particle size was increased due to the deposition, and then particles were covered by fuzz at the surface. Interestingly, the third stage was only observed in sequential D/He or He/D plasma exposure. No particle size increase was observed in D or He exposure until the particles were covered by fuzz. This may indicate that the synergistic effect of hydrogen and helium plays an important role.

4.2. The effect of D/He synergistic effect

H and He atoms coexist in the nuclear fusion reaction, and both have a significant impact on microstructure evolution. Recent research has shown that dual implantations of H and He show different effects on the microstructure evolution from single H or He implantations. Especially, the presence of He shows a significant trapping of H [26, 32].

In W matrix, the binding energy between H atom and monovacancy (Vac) is 1.28 eV, and the binding energy between He and monovacancy reached 4.57 eV, indicating that He is more likely to bind to vacancies and form the He-Vac complex. The H solution energy calculated using DFT shows that H solution energy near He-Vac is about 1 eV lower than that in the bulk, suggesting that the He-Vac complex can act as a trap that drives the H to segregate close to it. In addition, Zhou *et al* reported that no H_2 molecule forms inside a He-V complex, even the number of H atoms trapped by the complex is more than that by an He-free vacancy [33]. The reason may be that the additional volume occupied by He atoms disrupts the necessary conditions (the required space and optimal charge density) for the formation of H_2 molecules.

On the other hand, the binding energy between H and He_x-Vac complex (x is 1–4) is about 1 eV, which is comparable with H-Vac. The trapping energy per H atom inside a He-Vac complex is lower than that of H far away from the He-Vac complex when the number of captured H atoms is less than 13 [33]. Furthermore, the binding energy between He and H_xHe_y-Vac complex (x and y are 1–3) is 2.7–4.5 eV which is also comparable with He-Vac. This result indicates that the strong inaction between H and He suppressed their diffusion.

Overall, the synergistic effect of H and He is believed to have two main impacts: (1) higher He-defects binding energy hinder the formation of H_2 molecule and suppresses the formation of H bubble. (2) The strong inaction between H and He-defect clusters drives H to segregate close to He. Figure 21 shows the bubbles in the bottom of the fuzz layer with different exposure parameters. As we can see from figure 21(*a*), no visible bubbles in the bottom of the fuzz layer after D exposure. A bubble layer with a thickness of 300 nm was observed in He exposed sample with a dose of 5.0×10^{25} He m^{-2}, which was thicker than that in He/D (170 nm) or D/He (120 nm) exposed sample. This result confirms the rationality of the above analysis that the synergistic effect of hydrogen and helium suppresses the generation of bubbles.

This may also be one of the reasons for the different evolutions of particle size. The inhibition of bubble generation reduced the development of fuzz since the formation and growth of bubbles are important mechanisms for the formation of fuzz. At this point, the deposition process described in section 4.1 will become more dominant, resulting in a negative k and the particle evolution becoming deposition-controlled finally. Besides, it was also the reason why a thicker fuzz layer was observed in a single He exposed sample.

5. Conclusion

The present study systematically investigated the synergistic effect of deuterium and helium on the microstructure evolution behavior of W–Y_2O_3 material during plasma exposure. Based on the results and analysis, the following conclusions can be drawn:

(1) Y_2O_3 particles undergo a significant size change during plasma exposure, and this process was significantly influenced by the synergistic effect of hydrogen and helium. The visible size evolution of Y_2O_3 particles is controlled by three steps: the etching-controlled process at an initial stage, the deposition-controlled process when the sedimentation process becomes dominant, and the mixed controlled process.
(2) The fuzz structure on the surface of Y_2O_3 particles is composed of W instead of Y_2O_3, which is resulting from the deposition during plasma exposure.
(3) The synergistic effect of deuterium and helium has a significant impact on the microstructure evolution of W–Y_2O_3 material. The strong interaction between H and He-vacancy composite suppressed the bubble formation and growth, leading to a different evolutionary dynamic.

Acknowledgment

This work was supported by National MCF Energy R&D Program (2022YFE03140000), National Natural Science Foundation of China (12205071 and 12205070) and the Fundamental Research Funds for the Central Universities (JZ2023HGTB0213).

ORCID iDs

Jing Wang https://orcid.org/0000-0001-7346-8286
Laima Luo https://orcid.org/0000-0002-4455-7391

References

[1] Javadi S., Ouyang B., Zhang Z., Ghoranneviss M., Salar Elahi A. and Rawat R.S. 2018 Effects of fusion relevant transient energetic radiation, plasma and thermal load on PLANSEE double forged tungsten samples in a low-energy plasma focus device *Appl. Surf. Sci.* **443** 311–20
[2] Klein F., Litnovsky A., Wegener T., Tan X., Gonzalez-Julian J., Rasinski M., Schmitz J., Linsmeier C., Bram M. and Coenen J.W. 2019 Sublimation of advanced tungsten alloys under DEMO relevant accidental conditions *Fusion Eng. Des.* **146** 1198–202
[3] Xie X.F., Jing K., Xie Z.M., Liu R., Yang J.F., Fang Q.F., Liu C.S. and Wu X. 2021 Mechanical properties and microstructures of W–TiC and W–Y_2O_3 alloys fabricated by hot-pressing sintering *Mater. Sci. Eng.* **819** 141496
[4] Yao G., Liu X., Zhao Z., Luo L., Cheng J., Zan X., Wang Z., Xu Q. and Wu Y. 2021 Excellent performance of W–Y_2O_3 composite via powder process improvement and Y_2O_3 refinement *Mater. Des.* **212** 110249
[5] Hu W., Dong Z., Yu L., Ma Z. and Liu Y. 2020 Synthesis of W–Y_2O_3 alloys by freeze-drying and subsequent low temperature sintering: microstructure refinement and second phase particles regulation *J. Mater. Sci. Technol.* **36** 84–90
[6] Yao G., Luo L.-M., Tan X.-Y., Zan X., Xu Q., Zhu X.-Y., Lu E.-Y., Cao X.-Z., Cheng J.-G. and Wu Y.-C. 2019 Effect of Y_2O_3 particles on the helium ion irradiation damage of W–2%Y_2O_3 composite prepared by wet chemical method *Materialia* **6** 100268
[7] Lv Y., Zhao S., Han Y., Cheng H., Ye Z., Zhang H., Huang Y. and Fan J. 2022 The microstructure and radiation resistance of fine-grained W–0.3 wt%Y_2O_3 prepared by nano *in-situ* composite exposed to low-energy and high-flux helium plasma *J. Alloys Compd.* **903** 163927
[8] Qin W., Ren F., Doerner R.P., Wei G., Lv Y., Chang S., Tang M., Deng H., Jiang C. and Wang Y. 2018 Nanochannel structures in W enhance radiation tolerance *Acta Mater.* **153** 147–55
[9] Yao G., Zhao Z.-H., Luo L.-M., Cheng J.-G., Zan X., Xu Q. and Wu Y.-C. 2021 Damage evolutions of completely recrystallized W–Y_2O_3 composite evaluated using the dual effects of electron beam thermal shock and helium ion irradiation *Mater. Chem. Phys.* **271** 124947
[10] Huang J., Zuo T. and Wu Y. 2024 Evolution of irradiation damage in tungsten matrix and Y_2O_3 phase after low energy helium plasma exposure *J. Nucl. Mater.* **589** 154826
[11] Lee H.T., Haasz A.A., Davis J.W. and Macaulay-Newcombe R.G. 2007 Hydrogen and helium trapping in tungsten under single and sequential irradiations *J. Nucl. Mater.* **360** 196–207
[12] Wampler W.R. and Doerner R.P. 2009 The influence of displacement damage on deuterium retention in tungsten exposed to plasma *Nucl. Fusion* **49** 115023
[13] Liu X. *et al* 2017 Irradiation effects of hydrogen and helium plasma on different grade tungsten materials *Nucl. Mater. Energy* **12** 1314–8
[14] Yuan X., Hong S., Wang J., Ma B., Zhang Y., Niu M., Luo L. and Wu Y. 2025 A model to evaluate the ductile-to-brittle transition of bcc-W based on small tensile test and dislocation characterization *J. Alloys Compd.* **1011** 178483
[15] Zhang X., Qiao L., Zhang H. and Wang P. 2023 Influence of impurity gas seeding into deuterium plasma on the surface modification, sputtering erosion and deuterium retention in W and W-La_2O_3 alloy *Int. J. Hydrog. Energy* **48** 2075–89
[16] Medvedeva N.I., Zhukov V.P., Khodos M.Y. and Gubanov V.A. 1990 The electronic structure and cohesive energy of HfO_2, ZrO_2, TiO_2, and SnO_2 crystals *Phys. Status Solidi b* **160** 517–27
[17] Gusev M.I., Korshunov S.N., Suvorov A.L. and Lazarev N.E. 1999 Sputtering of tungsten, tungsten oxide, and tungsten-carbon mixed layers by deuterium ions in the threshold energy region *Tech. Phys.* **44** 1123–7
[18] Li L., Liu Z., Chen Z., Yin C., Mao S., Wu X., Ohno N. and Ye M. 2024 Surface modification of ZrC dispersion-strengthened W under low energy He plasma irradiation *Nucl. Fusion* **64** 056008
[19] Ueda Y. 2010 Status of plasma facing material studies and issues toward DEMO *Plasma Fusion Res.* **5** S1009

[20] Yao G., Tan X.-Y., Luo L.-M., Zan X., Xu Y., Xu Q., Zhu X.-Y., Tokunaga K. and Wu Y.-C. 2020 Influence of helium ion irradiation damage behavior after laser thermal shock of W–2%vol Y_2O_3 composites *Prog. Nucl. Energy* **121** 103241

[21] Guseva M.I., Gureev V.M., Kolbasov B.N., Korshunov S.N., Martynenko Yu V., Petrov V.B. and Khripunov B.I. 2003 Subthreshold sputtering at high temperatures *JETP Lett.* **77** 362–5

[22] Martynenko Y.V. and MYu N. 2012 Model of fuzz formation on a tungsten surface *Plasma Phys. Rep.* **38** 996–9

[23] Wu Y., Ni W., Fan H., Liu L., Yang Q., Cao B. and Liu D. 2016 Effects of He^+ energy and irradiation temperature on W sputtering yields under fusion-relevant conditions *J. Nucl. Mater.* **470** 164–9

[24] Federici G. *et al* 2001 Plasma-material interactions in current tokamaks and their implications for next step fusion reactors *Nucl. Fusion* **41** 1967

[25] Hammond K.D. 2017 Helium, hydrogen, and fuzz in plasma-facing materials *Mater. Res. Express* **4** 104002

[26] Xia T., Jiang Z., Wang Z., Shi Y., Ren X., Wang M., Liang L. and Zhu K. 2023 Interaction between hydrogen and helium in tungsten successively exposed by helium and hydrogen plasma *J. Nucl. Mater.* **574** 154184

[27] Causey R.A., Doerner R., Fraser H., Kolasinski R.D., Smugeresky J., Umstadter K. and Williams R. 2009 Defects in tungsten responsible for molecular hydrogen isotope retention after exposure to low energy plasmas *J. Nucl. Mater.* **390–391** 717–20

[28] Jia Y.Z., De Temmerman G., Luo G.-N., Xu H.Y., Li C., Fu B.Q. and Liu W. 2015 Surface morphology and deuterium retention in tungsten exposed to high flux D plasma at high temperatures *J. Nucl. Mater.* **457** 213–9

[29] Chen H. *et al* 2022 Effect of surface quality on hydrogen/helium irradiation behavior in tungsten *Nucl. Eng. Technol.* **54** 1947–53

[30] Achra S. *et al* 2021 Enhancing interface doping in graphene-metal hybrid devices using H_2 plasma clean *Appl. Surf. Sci.* **538** 148046

[31] Wang L., Zhou H.-S., Liu H.-D., Qi Q., Tu H.-J., Shi L.-Q. and Luo G.-N. 2022 The effect of He-induced surface microstructure on D plasma-driven permeation through RAFM steel *Nucl. Fusion* **62** 086006

[32] Lu G.-H., Zhou H.-B. and Becquart C.S. 2014 A review of modelling and simulation of hydrogen behaviour in tungsten at different scales *Nucl. Fusion* **54** 086001

[33] Zhou H.B., Liu Y.L., Jin S., Zhang Y., Luo G.N. and Lu G.H. 2010 Towards suppressing H blistering by investigating the physical origin of the H–He interaction in W *Nucl. Fusion* **50** 115010